Chapter-4

Electrocatalytic behaviour for $Sm_{2-x}Sr_xNiO_{4-\delta}$ (x = 0.4 to 1.0) Ruddlesden Popper based system

Publication: ***Manisha Chauhan, Pardeep K. Jha, Priyanka A. Jha* and Prabhakar singh****, ***"Influence of crystalline phase on electrocatalytic behaviour for Sm2-xSrxNiO4-δ (x = 0.4 to 1.0) Ruddlesden popper based system: A comparative study of bulk and thin electrocatalysts"*** *Phys. Chem. Chem. Phys., vol. 24, no. 9, pp. 5330–5342, 2022.*

CHAPTER 4: Electrocatalytic behaviour for $Sm_{2-x}Sr_xNiO_{4-\delta}$ (x = 0.4 to 1.0) Ruddlesden Popper based system

4.1 Introduction

For sustained and non-polluting energy cycles, attempts are made to promote photo-induced splitting of water into O_2 and H_2 as these two energy species from half reactions are combined in fuel cells to release energy and water regeneration. However, the water oxidation can produce peroxides, superoxide and hydroxyl radicals, reducing the process to an irreversible process and decreasing the overall performance. Hydrogen evolution reaction (HER) through water reduction catalysts is a well understood phenomenon. On a comparative note, there are fewer studies on water reduction catalysts and oxygen evolution reaction (OER), the complementary half-reaction of HER[58],[143],[144]. Thus, the structural and electronic properties of molecular catalysts, oxide/hydroxide catalysts with hybrid derivatives, composite materials and their isomorphic substitution along with doping are investigated for efficient catalysts[61], [155], [157], [158].

As active site engineering involves the size control, researchers have explored nano structured materials for electrocatalysts in order to promote kinetically sluggish OER. For this, transition-metals, layered hydroxides, metal organic frameworks, transition metal oxides, nanomaterials such as ZnO, TiO_2 etc., sulfides and nitrides and 3D transition metal elements inclusive of Co,Ni, and Fe are explored as OER catalysts due to their potential activity and stability[159]. RuO_2, IrO_2 [160]–[162], earth abundant metals (Mn, Fe, Co and Ni)[163]–[166], oxides, perovskite oxide [155],[156], phosphates [169]–[171], chalcogenides[172]–[174], hydroxides [175], [176] and borates [169], [177] have been extensively studied as OER catalysts. The scarcity and instable catalytic performance limit the use of RuO_2 and IrO_2 as OER catalysts in acidic medium. Further, the OER activities of single metal oxides are low and follow the order of decreasing activity as NiOx> CoO_x > FeO_x > MnO_x in alkaline medium [178]. In case of graphene, defects created by removal of hydrogen effectively enhance Oxygen Reduction Reaction (ORR), OER and Hydrogen Evolution Reaction (HER)[179]. $NiCo_2O_4$ 2D Nanosheets have shown improved reactivities with the increase in number of active sites[179]. Further, perovskites are also known to show OER with four electron transfer[180]. $CaMnO_{2.5}$ has shown higher OER than $CaMnO_3$ with the creation of molecular oxygen vacancies and high spin level configuration[181]. The A-site deficiency in $LaFeO_3$ significantly increased ORR and OER electrocatalytic activities [182]. The electrocatalytic performance can be improved by increasing the number of active sites and reactivity. Thus, number of active sites can be enhanced by creating oxygen vacancies either at the surface or interface. Further, high performance novel OER catalysts are required through fundamental understanding of the structure – property correlation of the catalyst surface in order to increase efficiency. However, electrocatalysts with high performance in neutral conditions (environment friendly) are required.

As mentioned in chapter 1, the Ruddlesden Popper perovskites (RP perovskites) have shown electrocatalytic properties along with excellent performance in oxygen-solid oxide fuel cell Hydrogen-solid oxide fuel cell[135]. Their performance is basically attributed to fast surface oxygen exchange property and proton and oxygen transport mechanism. The oxygen transport is basically occurring via here mechanisms: interstitial mechanism, interstitially mechanism and vacancy diffusion mechanism. The proton transport mechanism is mainly explained through Grothus mechanism of perovskites. The crystal structure, conductivity, TEC and ion transport can be specially regulated by doping the chemical element composition of simple RP perovskites[135]. The OER mechanism of RP perovskites is more complex and therefore, the effect of the defect chemistry and transport property on the ORR kinetics should be studied.

The RP perovskites with general formula $Ln_2NiO_{4-\delta}$ are charge ordering systems where charge ordering is governed by excess oxygen and is very sensitive to oxygen stoichiometry largely affected by the type of dopant[183]. The hole (Sr) substitution in $Ln_{2-x}Sr_xNiO_{4-\delta}$ (where δ is oxygen deficiency) causes a considerable change in lattice cell constant leading to the phase change. $Sm_{2-x}Sr_xNiO_{4-\delta}$ showed a transition from orthorhombic *Fmmm*(69) to tetragonal *I4/mmm*(139) around x = 0.7 due to the decrease in NiO_6 octahedron distortion and increase in Ni-O bond length[183]. The charge ordering behaves differently in different structural symmetries and affects the conductivity and electrocatalytic properties as well [184], [185]. It is also reported that the electrochemical studies evidence the role of protons in $Pr_2NiO_{4-\delta}$ in contrast to $Pr_{2-x}Sr_xNiO_{4+\delta}$ oxides. It is also concluded that in this nickelate $Pr_2NiO_{4+\delta}$ triple mixed conductivity (i.e. protonic, ionic as well as electronic conductivities) exists and with Sr^{2+} substitution protonic conductivity vanish and leads to the formation of gases[185]. This phenomenon is also observed in the present case of $Sm_{2-x}Sr_xNiO_{4+\delta}$.

The RP perovskites based electrocatalysts are synthesized using various techniques such as solid-state reaction method (SSR), molten salt synthesis, hydrothermal method, sol-gel, auto combustion method etc. To synthesize RP nickelates such as $Sm_{2-x}Sr_xNiO_{4+\delta}$, solid state reaction method is preferred because its synthesis using molten salts or combustion methods NiO_x gas is released which is harmful and toxic[186]. Thus, these compounds are synthesized using SSR technique. Pulsed Laser technique (PLD) is one of the techniques employed for the fabrication of thin films. It is the technique which is employed to fabricate high quality crystalline thin films. Thus, RP perovskites thin films are fabricated using PLD in order to maintain the crystallinity of the samples.

The literature review discussed in details in chapter 1 reveals that compositional variation on the kinetics of OER of Ruddlesden Popper layered structured oxides is least investigated and $Sm_{2-x}Sr_xNiO_{4-\delta}$ are least studied for their catalytic mechanisms at the triple phase boundary[167], [184]. In order to understand the insight mechanism of electrocatalytic behaviour with phase and dimension, we have studied the compositional effect along with the thin films. For this, we have synthesized $Sm_{2-x}Sr_xNiO_{4-\delta}$ (x= 0.2, 0.4, 0.6, 0.8 and 1.0) using conventional solid-state route to form two structures viz. tetragonal and orthorhombic with the change in oxygen stoichiometry. The thin films for x = 0.6 and 1.0 are prepared using PLD technique to study the OER and electrochemical reversibility [187]–[189] with the reduction in thickness, to check their suitability.

4.2 Experimental Procedure

4.2.1 Synthesis Technique

The $Sm_{2-x}Sr_xNiO_{4-\delta}$ ceramic samples (x = 0.4 – 1.0 at the steps of 0.2) were prepared by conventional solid state reaction process with initial reagents samarium oxide (Sm_2O_3), Strontium carbonate ($SrCO_3$) and Nickel Oxide (NiO) of purity > 99% weighed in stoichiometric amount and mixed thoroughly to obtain uniform dense ceramics. The molar ratio of the used precursors is shown in Table 4.1. The samples were then calcined in the alumina crucible in air at 1200 ˚C for 3h. The resultant calcined powder was then ground in an agate mortar and mixed with 2% polyvinyl alcohol (PVA) as a binder and then pelletized via 12 mm diameter cylindrical die-set under a hydraulic pellet press by applying uniaxial pressure of 5 tons/m^3 and then resulting pellets were sintered at 1425 ˚C temperature for 3 h at the heating rate of 5˚/min in air. Further, the epitaxial thin films of RP-type Nickelate ($Sm_{2-x}Sr_xNiO_{4-\delta}$: x = 0.6, 1.0) were grown on silica (SiO_2) substrate of dimension (1.5 cm ×1.0 cm ×2 mm) by using Pulsed Laser Deposition Technique (PLD) utilizing KrF excimer Laser (λ = 245 nm)[190]. The laser power was 438 mJ and 435 mJ for SSN0.6 and SSN1.0 thin film respectively and repetition rate was 5 Hz. The substrate temperature was kept at 700°C during deposition and number of shots were 1000 in each case.

Sample Phases	Elements	0.4 (1gm)	0.6 (1gm)	0.8 (1gm)	1.0 (1gm)
Bulk	Sm_2O_3	0.6739	0.5970	0.5185	0.4379
	$SrCO_3$	0.1434	0.2186	0.2952	0.3736
	NiO	0.1821	0.1844	0.1867	0.1891
Thin Film	Sm_2O_3		0.5970		0.4379
	$SrCO_3$		0.2186		0.3736
	NiO		0.1844		0.1891

Table 4.1: Molar ratio of the chemicals used for the synthesis of $Sm_{2-x}Sr_xNiO_{4-\delta}$ (x = 0.4-1 at the steps of 0.2)

4.2.2 Characterization techniques

The phase purity of samples was determined by X-Ray powder diffraction pattern (Rigaku Miniflex II desktop) with Cu-Kα radiation (λ ~ 1.5406 Å) at room temperature in the range 20° -70° with a step of 0.01. The phase formation of thin films was determined by X-Ray powder diffraction pattern (Bruker D8 Advance) with Cu-Kα radiation (λ ~ 1.5406) at room temperature in the range 20°- 70° with a step of 0.01. The surface morphology and EDX measurements was analyzed using scanning electron microscopy (EVO – Scanning Electron Microscope MA15/18). The dc conductivity is determined using Keithley electrometer 6517B meter in the temperature range of 20 – 700 ˚C at the step of 5 ˚C with the dc voltage of 1V using two probe methods. The electrochemical performance of the bulk samples and thin films was studied using Keithley 2450 source meter using three - electrode electrochemical system, where Ag/AgCl electrode used as reference electrode, Pt wire as a counter electrode, $Sm_{2-x}Sr_xNiO_{4-\delta}$ (x = 0.4 to 1.0) used as working electrode directly and 1M Sodium Sulphate (Na_2SO_4) used as electrolyte (pH = 7). A few consecutive voltammogram curves were recorded and specific capacitance was calculated. Using the Tafel approach the current corrosion rate was calculated. To study the weight loss the TGA measurement (Mettler Toledo, Germany) was performed in Nitrogen atmosphere at a heating rate of 5 ˚C min^{-1} in the temperature range from 30 to 1000 ˚C. The Fourier Transform infrared (FTIR) spectroscopy was performed via Nicolet iS5 using Attenuated Total Reflection (ATR) mode in the spectral range of 550 to 2000 cm^{-1}. The Chemical and elemental compositions of the surface of these samples were analyzed by using an X-ray photoelectron spectroscopy (KRATOS, Amicus model) a high-performance analytical instrument under 10^{-6} pa pressure using Mg target.

4.3 Results and Discussion

4.3.1 Structural and electrical Studies

Fig. 4.1 depicts the X-ray diffractograms of the sintered pellets of $Sm_{2-x}Sr_xNiO_{4-\delta}$ (x = 0.4 to 1 at the steps of 0.2) samples. The samples are observed in a single phase with some extra peaks indexed in the right part of Fig.4.1. These other peaks correspond to Sm_2O_3 according to PCPDF # 84-1878. With the increase in SrO, Sm_2O_3 remains as an unreacted precursor up to x = 0.6. Thereafter, it diminishes and at x = 1, the compound is pure phase and the mechanism can be illustrated in the equation (4.1)

$$(2-x)Sm_2O_3 + 2xSrO + 2NiO + \frac{x}{2}O_2 \rightarrow 2Sm_{2-x-\delta}Sr_xNiO_{4-\frac{3\delta}{2}} + \delta Sm_2O_3 + Sm_{Sr}^{\bullet} + V_{Sr}' \quad (4.1)$$

It can be seen that there is splitting in the peak corresponding to 2θ ~ 44° at x = 0.4 and this splitting is converting into two peaks at x = 0.8 and 1.0. The individual peak corresponding to 2θ ~ 59° at x = 0.4 is splitting at x = 1.0. Also, the individual peak at 2θ ~ 48° is observed to split at x = 1.0. These observations bring to quest regarding any phase conversion with x. The X-ray diffraction pattern of the sintered $Sm_{2-x}Sr_xNiO_{4-\delta}$ pellets (x = 0.0 and 0.2) in Fig.4.2 indicates that phase formation is not taking place for these two compositions.

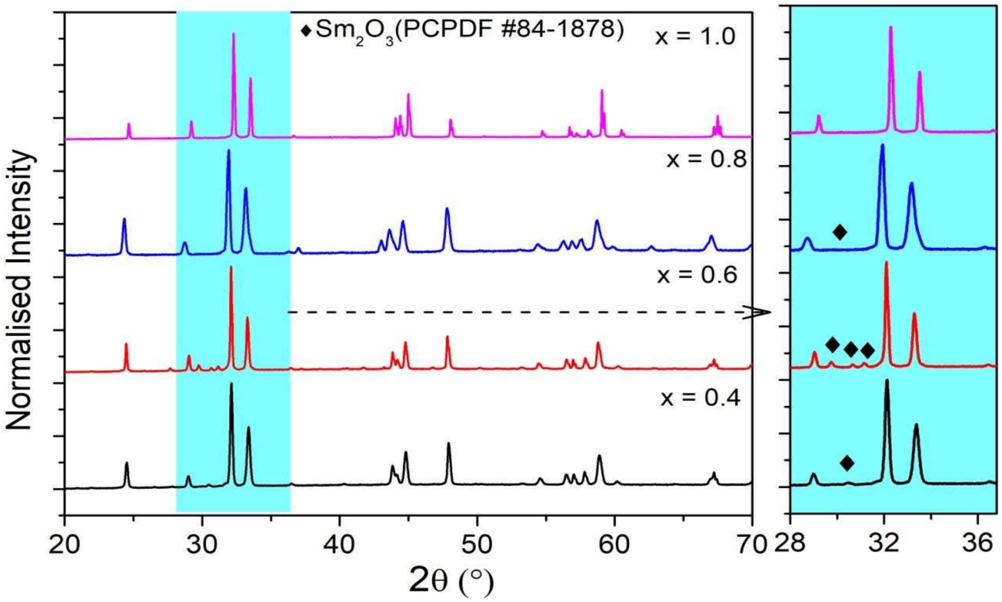

Figure.4.1: depicts the X-ray diffractograms of the sintered pellets of $Sm_{2-x}Sr_xNiO_{4-\delta}$ (x = 0.4-1.0 at the steps of 0.2) samples (Right panel) shows the formation of secondary phase.

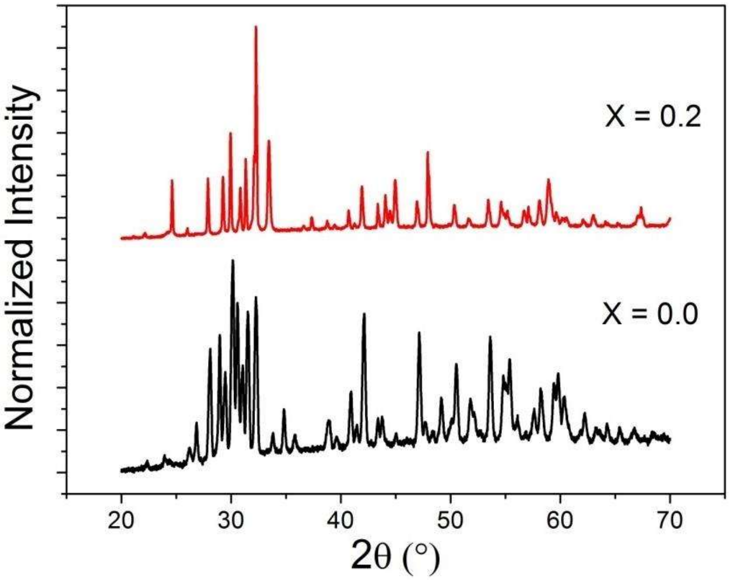

Figure.4.2: depicts the X-ray diffractograms of the sintered pellets of $Sm_{2-x}Sr_xNiO_{4-\delta}$ (x = 0.0 and 0.2)

The X-ray diffractograms showed the presence of some extra peaks. Thus, the phase purity of all the samples is determined by the formula:

$$\phi_{purity} = \frac{Ip}{Ip+0.8Is} \quad (4.2)$$

where Ip represents the maximum intensity of primary peak and I_S represents the maximum intensity of the secondary phase. The phase purity is depicted in Fig. 4.3 (a). From the graph it is clear that the phase purity decreases with Sr substitution up to x = 0.6 and thereafter, it increases to 100% for x = 1.0. The Microstrain caused by crystalline defects has been calculated from Rietveld refinement of XRD results by using Williamson–Hall model. The Williamson– Hall model is given by $\beta cos\theta = 0.9\frac{\lambda}{t} + 4 \in sin\theta$ where t is average crystallite size and ∈ is microstrain, β is the full width at half maxima (FWHM) at Bragg's angle (2θ) and λ being the X-ray wavelength of Cu Kα (k = 1.54098 Å). The slope and intercept of βcosθ vs 4 sinθ curve (graph not shown here) gives the value of microstrain and crystallite size, respectively. Fig. 4.3(a) shows the variation of microstrain with x. It is observed that the value of microstrain decreases with x for x = 0.4 and 0.6 in orthorhombic region. Further, with the phase change, from x= 0.6 to 0.8, it increases from orthorhombic to tetragonal (illustrated through cyan rectangle in Fig. 4.3(a) and further decreases with x = 1.0. Thus, the behavior of microstrain resembles the phase transition behavior.

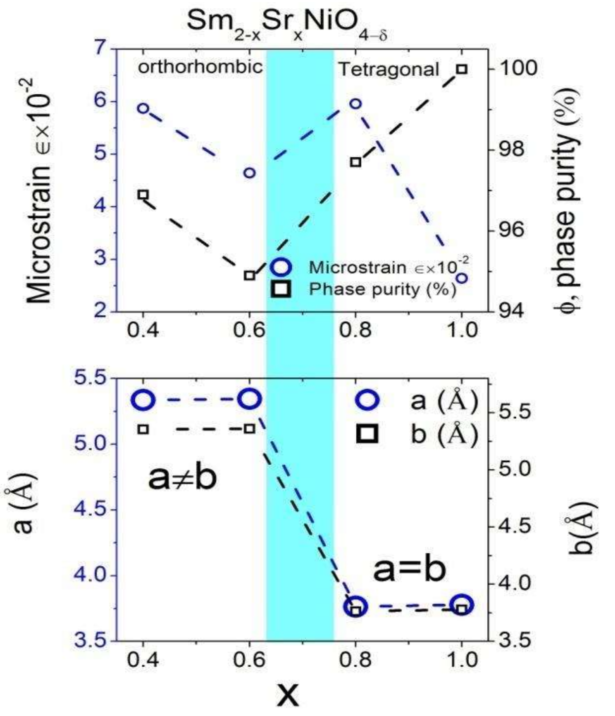

Figure.4.3: (a) Variation of microstrain and phase purity with x for the studied samples $Sm_{2-x}Sr_xNiO_{4-\delta}$ (x = 0.4-1.0 at the steps of 0.2). (b) Lattice parameters obtained from Rietveld refinement of the X-ray diffractograms.

Fig.4.3(b) shows the variation of lattice parameters obtained after Rietveld refinement of the X-ray diffractograms with x. It is observed that the lattice parameters a (5.33 Å) ≠ b (5.35 Å) for the orthorhombic phase and for tetragonal phase a (3.76 Å) = b (3.76 Å).

The Rietveld refinement of the XRD pattern (bulk $Sm_{2-x}Sr_xNiO_{4-\delta}$ samples) obtained at room temperature is done with orthorhombic F*mmm* and tetragonal I*4/mmm* symmetry using

Full prof software using peak profile Thompson–Cox–Hastings pseudo-Voigt function with axial divergence symmetry and instrumental correction (Fig.4.4(a)). The values of goodness of fit factor showed that they lie within acceptable range ($\chi^2 \leq 10$) and confirm orthorhombic F*mmm* symmetry for x = 0.4 and 0.6 and tetragonal I*4/mmm* symmetry for x = 0.8 and 1.0. Fig.4.4(b) also showed the splitting of the peaks changing with x and the matching of peak profile according to the corresponding symmetries. Further, the lattice positions, R-factors obtained after refinement are illustrated in Table 4.2 and the corresponding unit cell structure is shown in Fig. 4.4(c). The XRD patterns reveal the phase conversion with x and this is in accordance with the previous reported results[135] that phase conversion from orthorhombic to tetragonal takes place around x = 0.7. This structural change with Sr substitution occurs due to the displacement of atoms from their regular lattice positions as the bond length has altered from 1.8891 Å to 1.8925 Å in orthorhombic phase. This leads to structural and microstructural changes and transformations in crystallite size (Fig. 4.1- 4.3). The elemental concentration plays an important role in the transport and catalytic behaviour of materials, variation of Ni content and the ratio of Ni/(Sm+Sr) (ratio of B-site/A-site) obtained from EDX is shown in Fig.4.4(d). In the orthorhombic phase ($0.4 \leq x < 0.8$), Ni content increases with the increase in x. Whereas in tetragonal phase ($x \geq 0.8$), with the increase in x Ni content decreases. While, the ratio of Ni/(Sm+Sr) is observed to vary in correlation with Ni. The stoichiometric ratio is least deviated for composition with x = 0.6. However, the composition x = 0.6 and 0.8, do not show any significant difference in the conductivity for temperature < 500 K as observed in Fig.4.4 (e), which depicts the Arrhenius plot for the studied $Sm_{2-x}Sr_xNiO_{4-\delta}$ (x = 0.4 - 1 at the steps of 0.2) samples. The black coloration of compounds on heating during the synthesis (Fig. 4.4(e) inset) confirms of presence of Ni^{3+}. On the basis of charge compensation, Ni^{3+} content should be in correlation with oxygen deficiency till the structure remains unchanged. Thus, we expect maximum Ni^{3+} content for x = 0.8 as observed in Fig.4.4(d). It is also observed that the conductivity increases with x with high conductivity for x = 1. However, conductivity is very low at room temperature showing nearly insulating behaviour with the exception of x =1.0 which possess excess of oxygen along with maximum hole substitution[191]. Hence, we have performed the comparative catalytic study to investigate the OER mechanism for the most stoichiometric composition i.e., x = 0.6 (with least i.e., oxygen deficiency) and the most conductive with excess of oxygen i.e., x = 1.0 (is negative).

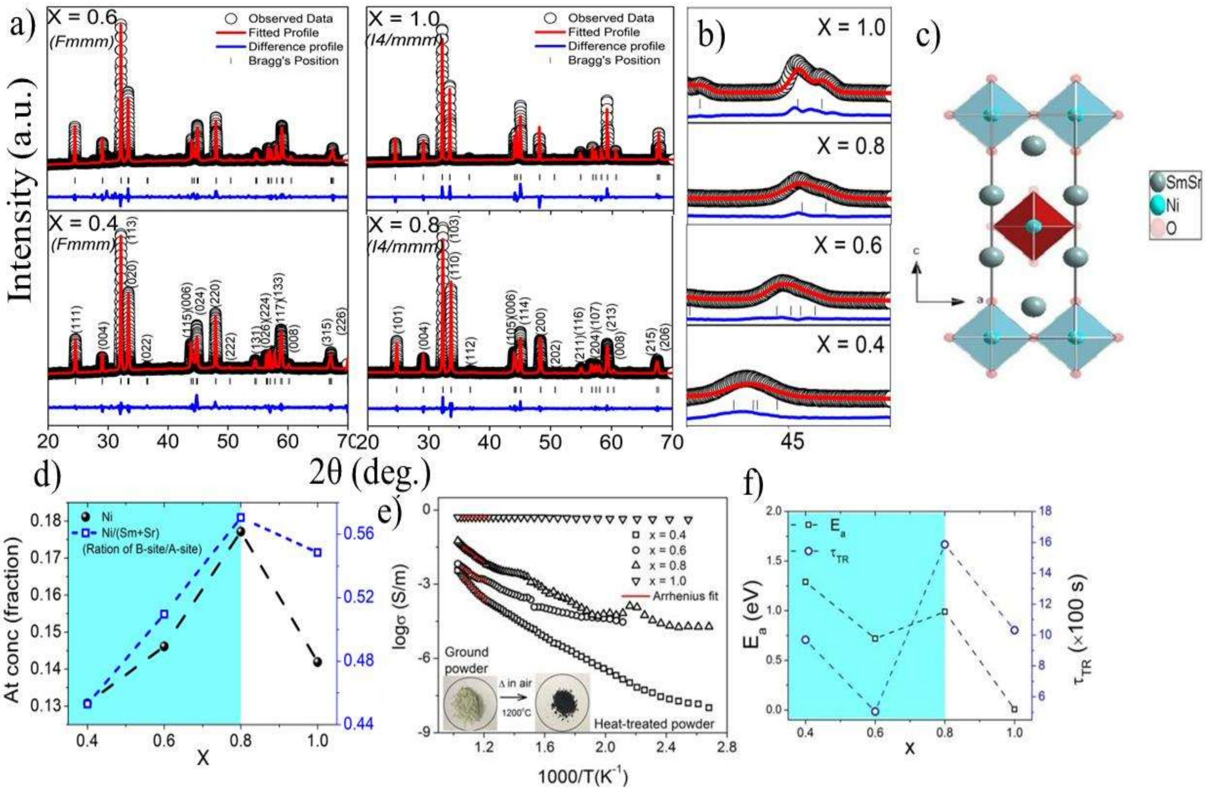

Figure.4.4: (a) Rietveld refinement of the X-ray diffractograms of the studied samples $Sm_{2-x}Sr_xNiO_{4-\delta}$ (x = 0.4 - 1 at the steps of 0.2). It is seen from that x = 0.4 and 0.6 show orthorhombic Fmmm symmetry and x = 0.8, 1.0 showed tetragonal I4/mmm symmetry (b) splitting observed at 2θ ~ 45° confirming the phase change (c) Tetragonal Structure of $SmSrNiO_{4-\delta}$ (d) Variation of Ni and ratio of Ni/(Sm+Sr) with x suggesting the compensation mechanism (e) Value of conductivity at 100 °C of bulk $Sm_{2-x}Sr_xNiO_{4-\delta}$;(e, inset) black coloration on heat treatment.

Sample	Atoms	Position coordinates			Occupancy	B($Å^2$)	R-factors	
		x	Y	z			R_{wp}	R_e
x = 0.4	Sm	0	0	0.36378	1	0.6431	9.14	6.53
	Sr	0	0	0.36378	1	0.9730		
	Ni	0	0	0	1	0.8833		
	O1	0.25	0.25	0	1	0.3930		
	O2	0	0	0.16314	1	0.4933		
x = 0.6	Sm	0	0	0.36236	1	0.6347	9.78	5.57
	Sr	0	0	0.36236	1	0.9621		
	Ni	0	0	0	1	0.7334		
	O1	0.25	0.25	0	1	0.4671		
	O2	0	0	0.16321	1	0.4543		
x = 0.8	Sm	0	0	0.36265	1	0.6349	11.6	5.34
	Sr	0	0	0.36265	1	0.9867		
	Ni	0	0	0	1	0.7576		
	O1	0.5	0	0	1	0.4977		
	O2	0	0	0.16967	1	0.4443		
x = 1.0	Sm	0	0	0.36754	1	0.6894	11.8	6.20
	Sr	0	0	0.36754	1	0.9664		
	Ni	0	0	0	1	0.7836		
	O1	0.5	0	0	1	0.4983		
	O2	0	0	0.16583	1	0.7557		

Table 4.2: Atomic positions and R-factors obtained after refinement for the $Sm_{2-x}Sr_xNiO_{4-\delta}$ (x = 0.4 to 1.0) samples

4.3.2 Thermogravimetric studies

The compensation mechanism and oxygen content for the bulk $Sm_{2-x}Sr_xNiO_{4-\delta}$ is verified using Thermogravimetric studies in N_2 atmosphere. In Fig.4.5 (a, b), a gradual weight loss (%) is observed for x = 0.4 and x = 0.6, while a peak is observed for x = 0.8 (Fig.4.5(c)) followed by the broad hump at x = 1.0 (Fig.4.5(d)). Further, two kinks are observed at x = 0.4 corresponding to the weight loss for CO and O_2 respectively. The peaks observed in x = 0.8 and x= 1.0 suggest the increase in oxygen content as there is increase in weight[144]. Further, the position of kinks is again estimated through the dm/dT curves shown in Fig.4.5(e, f, g and h). The position of kinks is in accordance with the position observed in mass loss curves. Also, peak profiles are observed to vary in the two different structures/ different δ as the oxygen deficiency is believed to lead the structural instability and commensurate/incommensurate changes [192]. Here, δ has varied from -0.19 to 0.077 for x = 0.6 and 1.0, respectively. Thus, structure change with x can be coupled with the change in oxygen non-stoichiometry with the alteration in structural energy and stability of $Sm_{2-x}Sr_xNiO_{4-\delta}$. This structure change is possible due to the change in NiO1 bond length and lattice parameter ‘a’ which is correlated with δ as higher δ reduces lattice size.

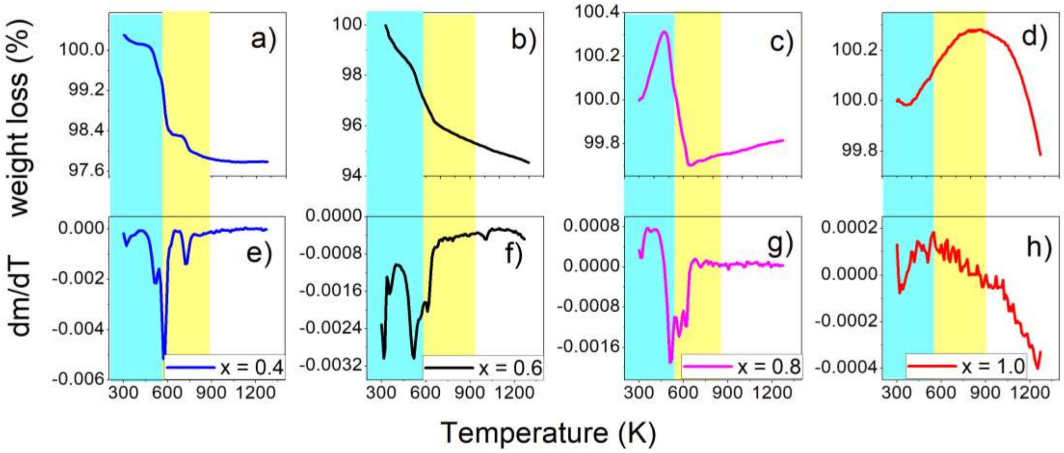

Figure 4.5: (a, b, c and d) Variation of weight loss (%) with temperature of the studied samples $Sm_{2-x}Sr_xNiO_{4-\delta}$ (x = 0.4 - 1 at the steps of 0.2). It is seen that structural change is governed with the oxygen non-stoichiometry (e, f, g and h) dm/dT curves with temperature of the studied samples $Sm_{2-x}Sr_xNiO_{4-\delta}$ (x = 0.4 - 1 at the steps of 0.2), the position of kinks and peaks are in accordance with the mass loss curves

4.3.3 Microstructural Studies

The microstructure and chemical composition of the $Sm_{2-x}Sr_xNiO_{4-\delta}$ (x = 0.4 - 1 at the steps of 0.2) samples are characterized by SEM and EDX analysis. Fig. 4.6 represents the SEM micrograph and their respective insets depict the grain size histograms for the studied samples. With the increase in x, the grain size is observed to increase. The features observed at the surface indicate the grain –growth stage (highly densified) of the studied samples. The EDX data of all samples show the presence of Sm, Sr, Ni, and Oxygen verifying the fact that the compound obtained is in stoichiometric compositions.

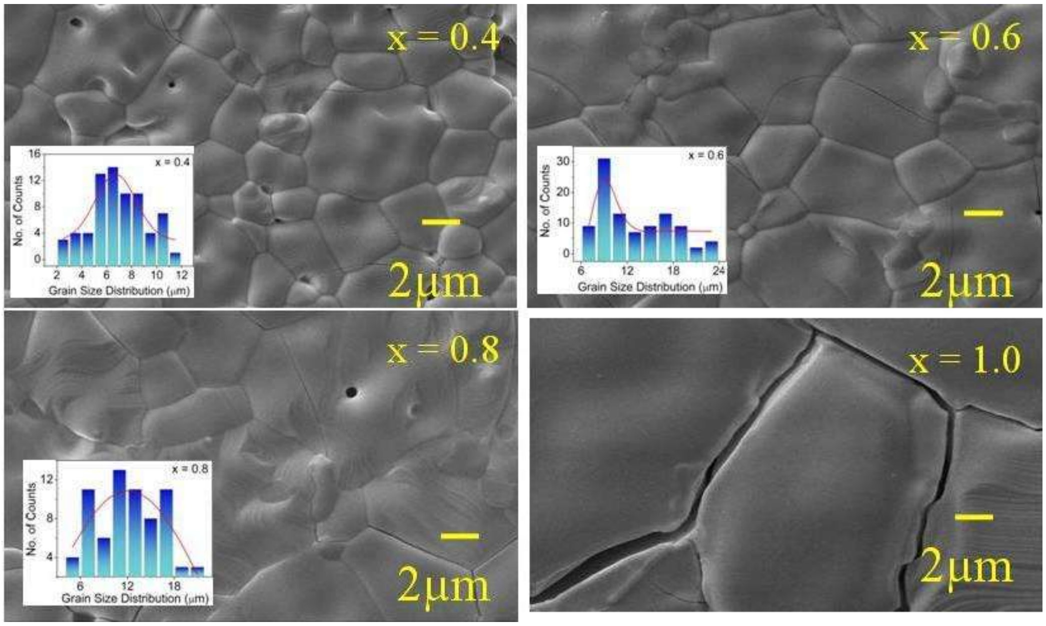

Figure.4.6: SEM micrographs and their respective insets depict the grain size histograms for the $Sm_{2-x}Sr_xNiO_{4-\delta}$ (x = 0.4 – 1.0 at the steps of 0.2)

4.3.4 Catalysis Studies

4.3.4.1 Bulk

In our recent studies [193], we had observed the effect of microstructure on the triple phase boundary and the change in number of electron transfer from $2e^-$ to $4e^-$ in $SmSrNiO_{4-\delta}$ (i.e., x = 1.0) with the sintering temperature from 1250 °C to 1425 °C. The electrocatalysis is believed to be affected with the structure change, we have studied the electrocatalysis for all the studied samples (Fig.4.8 for x = 0.4 and Fig.4.9 for x = 0.8) but presented here only for x = 0.6 and x = 1.0 in bulk $Sm_{2-x}Sr_xNiO_{4-\delta}$ on a comparative note with two structures orthorhombic and tetragonal, respectively. The reversible cyclic voltammetry is a phenomenon which is mainly governed by diffusion process but the conduction process comprises of Faradaic currents due to several phenomenon such as charge transfer, mass transfer etc. When reaction is controlled by charge transfer then diffusion and adsorption take place along with the desorption. Simultaneously, when the number of electrons change then electrochemical reversibility alters into partial and complete irreversibility[194]. This reversibility depends up on the scan rates and highest reversibility occurs at the slow scan rate. But this is not the case for multiple electron transfer. Figure 4.7(a) represents the cyclic voltammograms showing complex electrode mechanism followed by chemical reaction mechanism with the scan rate for x = 0.6 in bulk $Sm_{2-x}Sr_xNiO_{4-\delta}$ and with the increase in scan rate, peak splitting is observed with $\Delta E_p > 180$ mV suggesting the two-electron process [194]. Further, for x =1.0, there is a reduction in the height of the peak with $\Delta E_p \sim 57$ mV suggesting the electron transfer chain mechanism with the 4 electron process[190]. Further, with the scan rate area under the curve increases while, on a comparative note, for x = 0.6 and x = 1.0, area increases marginally for x = 1.0 than that of x = 0.6 (Fig. 4.7(b)). Randles-Selvick (RS) equation is used to check the electrochemical reversibility $i_p = 0.446nFAC^0\left(\frac{nFvD_o}{RT}\right)^{1/2}$ where F is Faraday constant, v is scan rate, R is gas constant, T is absolute temperature, A is electrode surface area, D_o is diffusion coefficient and C^0 is the bulk concentration. The peak current is plotted versus $v^{1/2}$ (Fig.4.7(c)). The plot is nearly linear for both the samples with the change is slope suggesting the diffusion mechanism. When number of electrons participate in the diffusion then this equation is modified as $i_p = \frac{n^2F^2}{4RT}vA\Gamma^*$ where n is number of electrons participating in the redox reaction, and Γ^* is the surface covered under adsorbed surfaces [195]. The log-log plot of the scan rate with current density is shown in Fig. 4.7(d) and slope lies between 0.5 and 1.0 suggesting the combination of diffusion and adsorption while major conduction is occurring through diffusion [194].

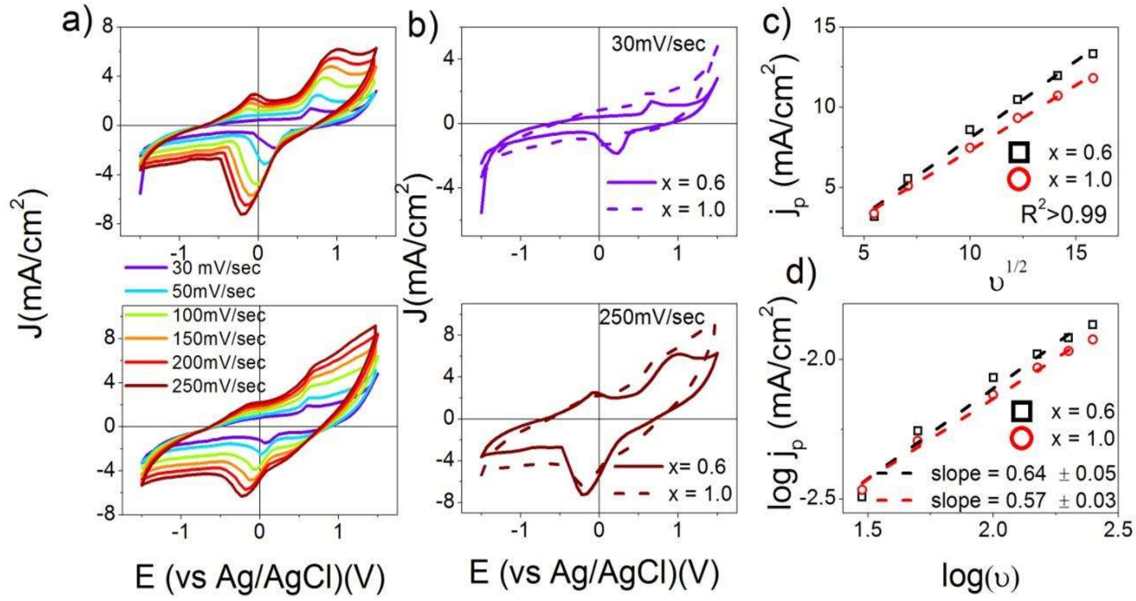

Figure 4.7 (a) represents the cyclic voltammograms showing ECE mechanism with the scan rate for x = 0.6 and ETC mechanism with the 4-electron process for x =1.0 (b) Variation of area with the scan rate for x = 0.6 and 1.0 (c) RS equation plot between the current density and √υ for x = 0.6 and 1.0 (d) log-log plot of current density and υ for the studied samples

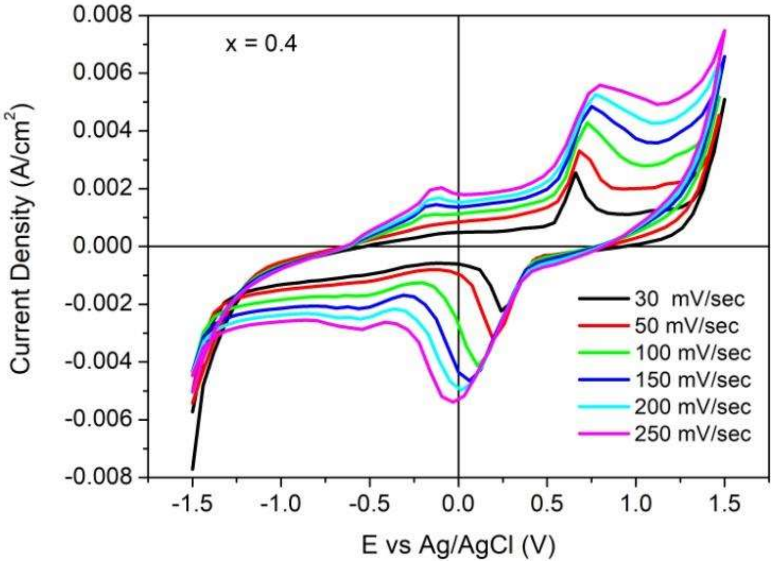

Figure 4.8: Cyclic Voltammograms with the scan rate of the $Sm_{2-x}Sr_xNiO_{4-\delta}$ (x = 0.4).

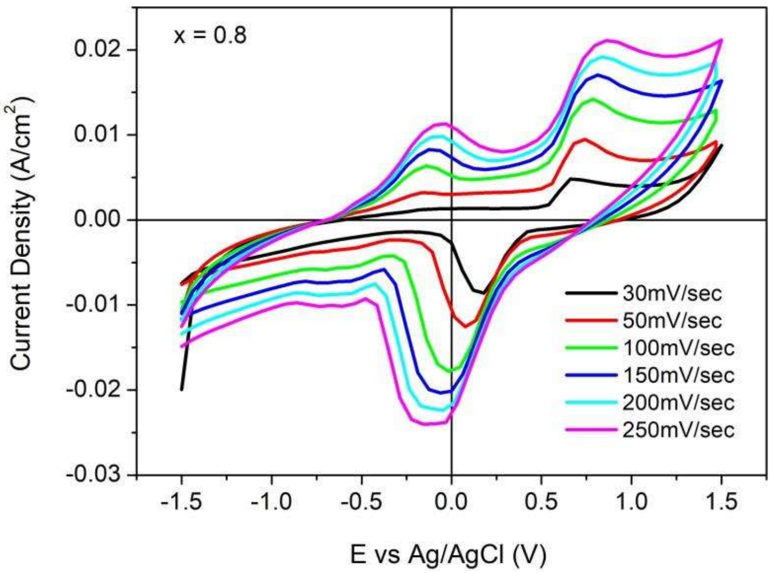

Figure 4.9: Cyclic Voltammograms with the scan rate of the $Sm_{2-x}Sr_xNiO_{4-\delta}$ (x = 0.8).

As observed, there is a reduction in the height of peak (Fig.4.7(b)) with the composition (structure) which leads to a quest regarding the reversibility or irreversibility index of the cyclic voltammograms. The reversibility or irreversibility is the index of life time of the redox couples participating in the reaction i.e., from electrode to solution or vice versa. It also occurs when the rate of interfacial electron transfer is slower than the mass transport. The Butler Volmer equation combined with Fick's law suggests expression for faradaic currents in terms of field where standard electrochemical potential, E^o, half peak potentials, $E_{p/2}$ and inflection points, E_i are used to estimate the reversibility and irreversibility[196]. The parameters (E^o, $E_{p/2}$, E_i) are extracted from the differential analysis of the voltammograms for the different scan rates in order to predict the reversibility/irreversibility with x. The first and second order derivative of CV curves of the studied samples for 30 mV/sec and 250 mV/sec is shown in Fig.4.10. It is observed that the peaks for forward and reverse scan are not exactly overlapped along with the shifting of peaks towards the lower potential with x suggesting partial irreversibility.

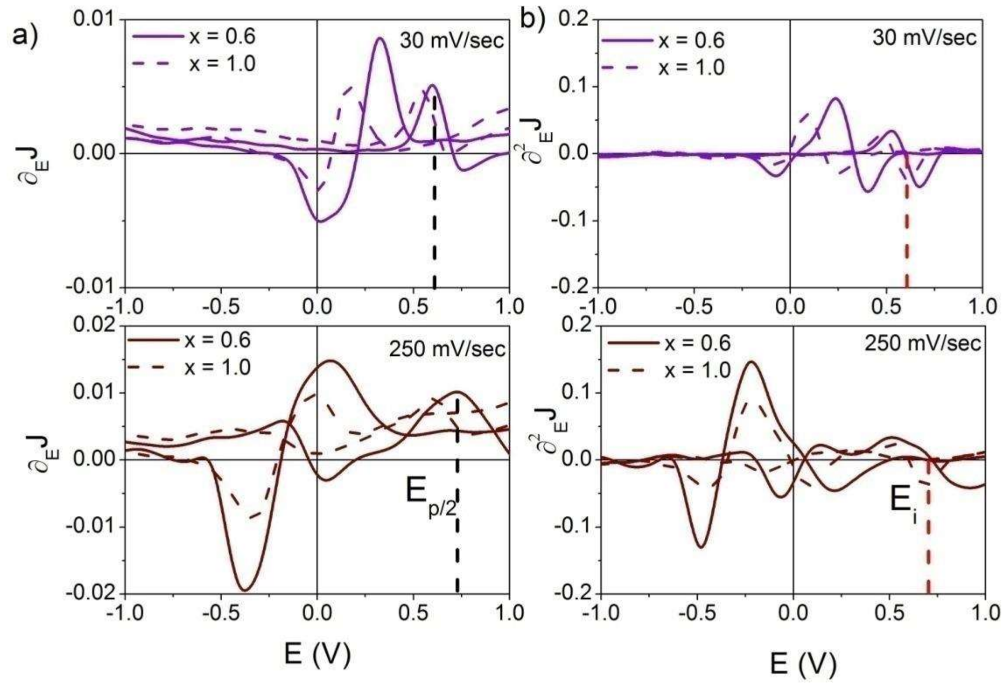

Figure 4.10: First and second order derivative CV curves showing $E_{p/2}$ (black dash lines) and E_i (red dash lines) of the studied samples for 30 mV/sec and 250 mV/sec for the estimation of parameters

Fig. 4.11 depicts the variation of $E_{p/2}$ and E_i (obtained from the single and double order derivatives of CV curves of bulk $Sm_{2-x}Sr_xNiO_{4-\delta}$) with the scan rate for the forward scans of x = 0.6 and 1.0. For x =1.0, $E_{p/2}$ and E_i are nearly overlapping with each other confirming the irreversible behaviour while for x = 0.6, $E_{p/2}$ and E_i overlap with each other for low scan rate and diverge from each other for the higher scan rates confirming quasi electrochemical irreversibility with the multiple electron transfer.

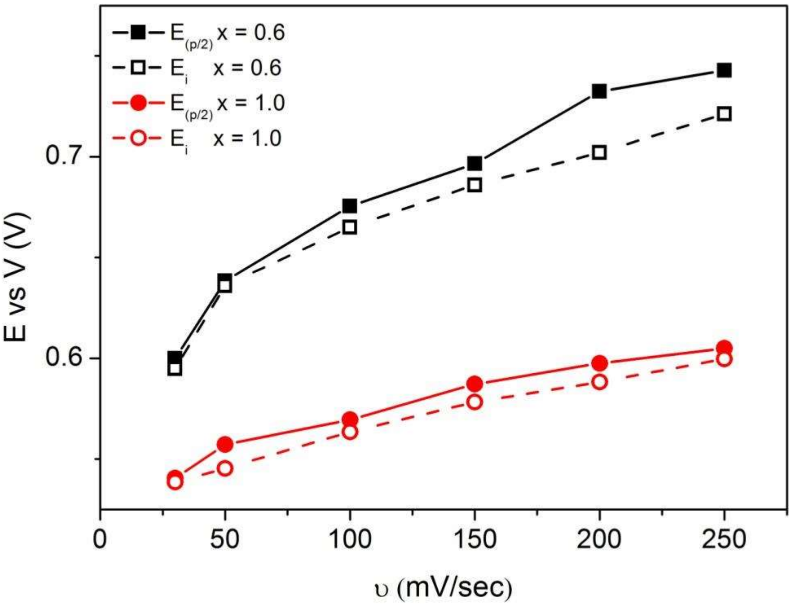

Figure 4.11: Variation of $E_{p/2}$ and E_i with the scan rate for the forward scans of x = 0.6 and 1.0.

Further, the thin films of the two structures are fabricated using PLD and their suitability is also checked as an electrocatalyst. A comparative of the mechanism of two structures in their bulk and nano forms is also studied.

4.3.4.2 Thin Film

The XRD pattern of the thin films of $Sm_{2-x}Sr_xNiO_{4-\delta}$ (x = 0.6 and 1.0) is shown in, Fig. 4.12. Further, a comparative of lattice mismatch, grain size, crystallite size is shown in Table 4.3. It is found with the compositional phase change; mismatch is very high. This mismatch induces strain resulting in drastically affecting the electronic properties [197]–[199]. In the present case, the grain size of thin film (for SEM micrographs and grain size histograms, Fig 4.13) is higher than that of their bulk counterparts but it is irrespective of the phase change in thin films. The crystallite size is smaller in case of x = 0.6 bulk as compared to x = 0.6 thin film. The dislocation density is higher in bulk sample as compared to their thin counterparts.

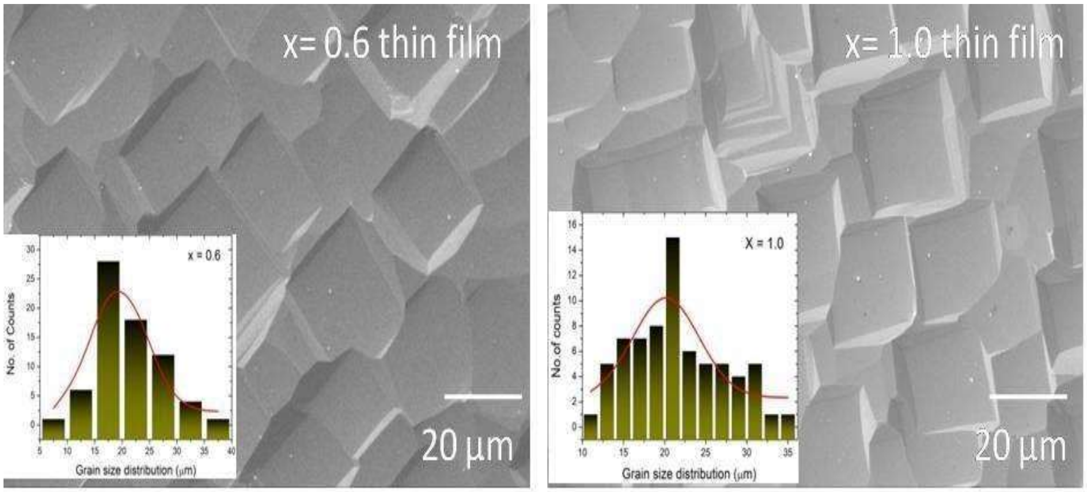

Figure 4.12: SEM micrographs and respective grain size histograms for the thin films of $Sm_{2-x}Sr_xNiO_{4-\delta}$ (x = 0.6, 1.0 thin film)

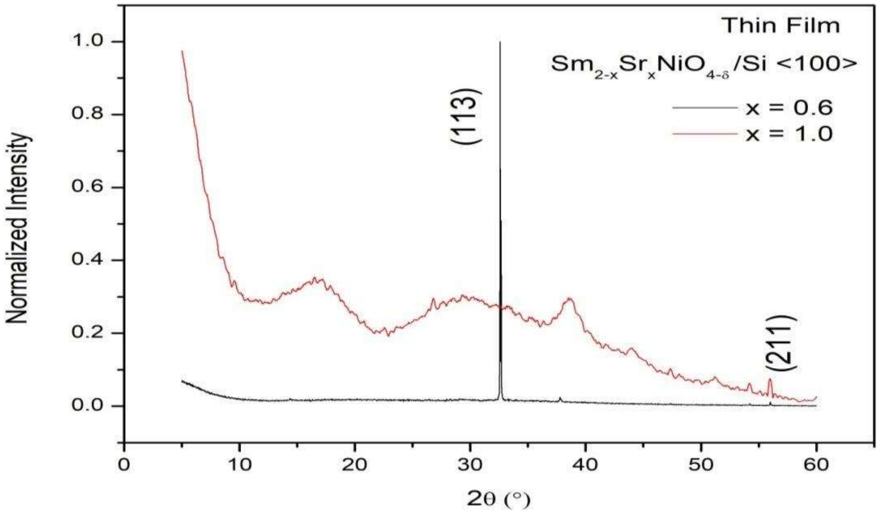

Figure 4.13: X-ray diffractograms of the films of $Sm_{2-x}Sr_xNiO_{4-\delta}$ (x =0.6 and x = 1) samples

Compositions	x = 0.6 Bulk	x=1.0 Thin Film	x = 1.0 Bulk	x = 0.6 Thin Film
Microstrain	4.64×10^{-4}	2.43×10^{-4}	2.64×10^{-4}	2.52×10^{-4}
Crystallite size (nm)	70.67	265.86	146.59	165.58
Dislocation Density(nm^{-2})	2.01×10^{-4}	1.42×10^{-5}	4.66×10^{-5}	3.65×10^{-5}
Grain Size (µm)	~10	~20	~20	~20
Lattice Mismatch	-	1.55%	-	30.40%

Table 4.3: A Comparison of lattice mismatch, grain size, and crystallite size for $Sm_{2-x}Sr_xNiO_{4-\delta}$(x = 0.6 and 1.0) bulk and thin films.

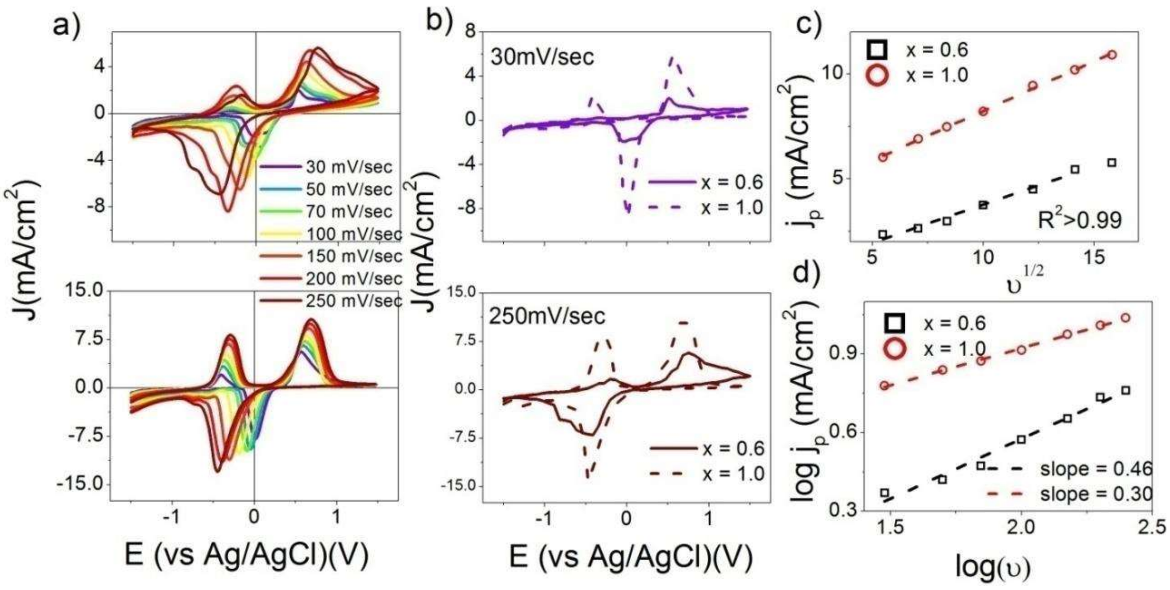

Figure 4.14 (a) represents the cyclic voltammograms with the scan rate for x = 0.6 and x =1.0 thin films (b) Variation of area with the scan rate for x = 0.6 and 1.0 thin films (c) RS equation plot between the current density and $\sqrt{\upsilon}$ for x = 0.6 and 1.0 thin films (d) log-log plot of current density and υ for the studied thin films

Figure 6(a) represents the cyclic voltammograms with the scan rate for x = 0.6 thin film and with the increase in scan rate, peak splitting is observed with ΔE_p > 180 mV suggesting the two-electron process[194]. Further, for x =1.0 thin film, there is no peak splitting with the increase in scan rate rather with the scan rate, peak position is observed to shift with the scan rate. Moreover, with the scan rate area under the curve increases and on a comparative note, area increases for x = 1.0 thin film than that of x = 0.6 thin film (Fig. 4.14(b)). To check the electrochemical reversibility, the peak current is plotted versus $v^{1/2}$ (Fig.4.14(c))[194] and the plot is nearly linear for both the thin films with the change in slope suggesting the diffusion mechanism. Further, the log-log plot of the scan rate with current density (Fig. 4.14(d)), slope is less than 0.5 suggesting that the major conduction is occurring through adsorption [194].

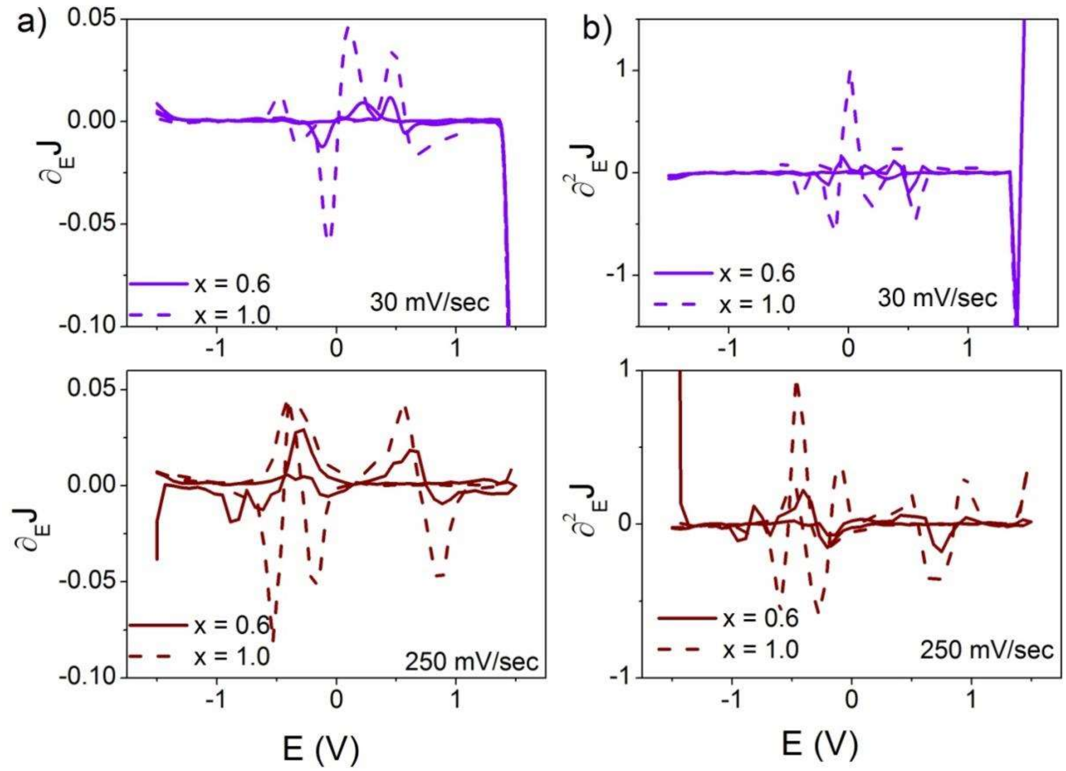

Figure 4.15: First and second order derivative CV curves for x = 0.6 and 1.0 thin films at 30 mV/sec and 250 mV/sec for the estimation of parameters $E_{p/2}$ and E_i

The first and second order derivative of CV curves for x = 0.6 and 1.0 thin films at 30 mV/sec and 250 mV/sec is shown in Fig.4.15. It is observed that the peaks for forward and reverse scan are not exactly overlapped and observed to shift towards lower potential. Further, there is shifting of peaks towards the lower potential suggesting partial irreversibility with x[196]. This variation is also observed in E_i with x.

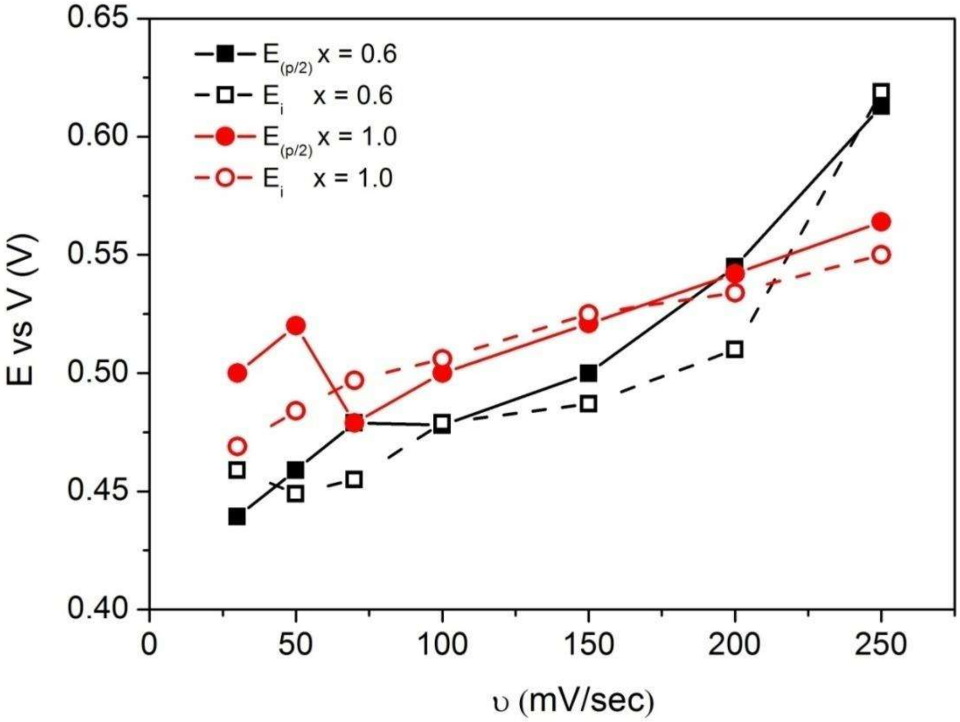

Figure 4.16: shows the variation of $E_{p/2}$ and E_i with the scan rate for the forward scans of x = 0.6 and 1.0 thin films

Fig. 4.16 shows the variation of $E_{p/2}$ and E_i with the scan rate for the forward scans of x = 0.6 and 1.0 thin films. In case of thin films for x = 0.6 and x = 1.0, $E_{p/2}$ and E_i are nearly overlapping with each other confirming the irreversible behaviour with the multiple electron transfer.

1.3 Comparative of Tafel slope for Bulk and thin films:

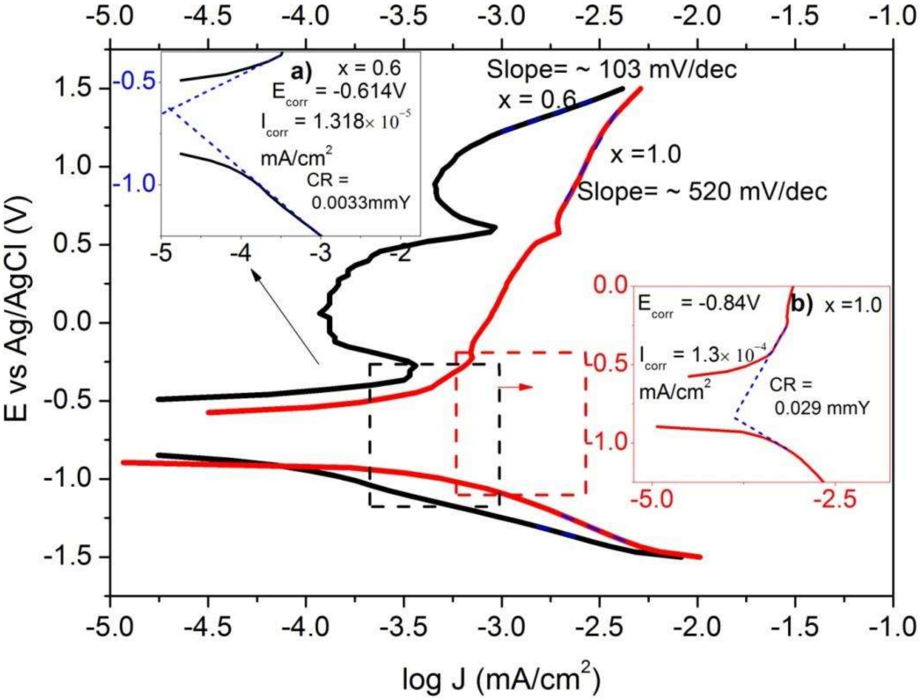

Figure 4.17: Tafel plot showing E vs Ag/AgCl (V) and log J (mA/cm^2) and the insets a) and b) correspond to the corrosion rates for x = 0.6 and 1.0, respectively.

The corrosion rate (CR) estimated from the Tafel plot by equation $CR\ (mm/y) = 3.27 \times I_{Corr}\left(\frac{mA}{cm^2}\right) \times (ew/d)$ where ew is equivalent weight and d is density of the material [192] (Fig. 4.17). It is observed that CR is lower for x = 0.6 (~ 0.0033 mm/year) than that for x = 1.0 (~ 0.029 mm/year) (insets (a) and (b)). Earlier[193], we have observed lower CR for the sample x =1.0 might be due to the different concentration of analyte. The different CR corresponds to the different passivation mechanism and different thickness of protective film developed over the cathode leading to the decrease in peak current. This is confirmed through the formation of different passive and transpassive regions in x = 0.6 sample.

The Tafel slope measured at the point of CR (insets) are ~90 mV/decade and 200 mV/decade for the x= 0.6 and 1.0, respectively. The Tafel slope of 90 mV/sec is confirming the conduction through two electron transfer in x = 0.6 sample [200]. This is a type of moderate catalyst where some active sites are available for four electron paths and some are available for the two electron paths (majorly). Further, higher Tafel slope is also observed in the transpassive regions for x = 1.0 (520 mV/decade).

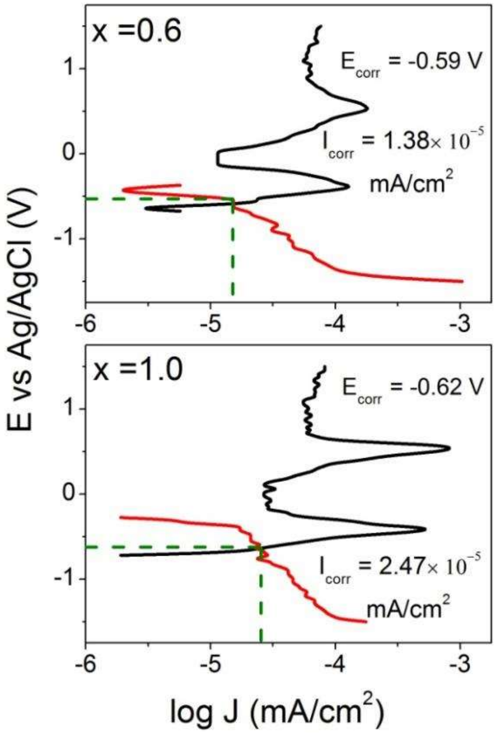

Figure 4.18: Tafel plot showing E vs Ag/AgCl (V) and log J (mA/cm^2) correspond to the corrosion rates for x = 0.6 and 1.0 thin films, respectively.

On a comparative note, the Tafel slope for the x = 0.6 and 1.0 thin films (Variation of (E vs Ag/AgCl(V)) vs log J is shown in Fig. 4.18. It is observed that I_{corr} is nearly double for x = 1.0 thin films instead of x = 1.0 bulk sample. The different CR correspond to the different passivation mechanism developed over the cathode. This is confirmed through formation of different passive and transpassive regions in x = 0.6 and x = 1.0 thin films. The Tafel slope calculated for thin films in the transpassive region is listed in Table 4.4.

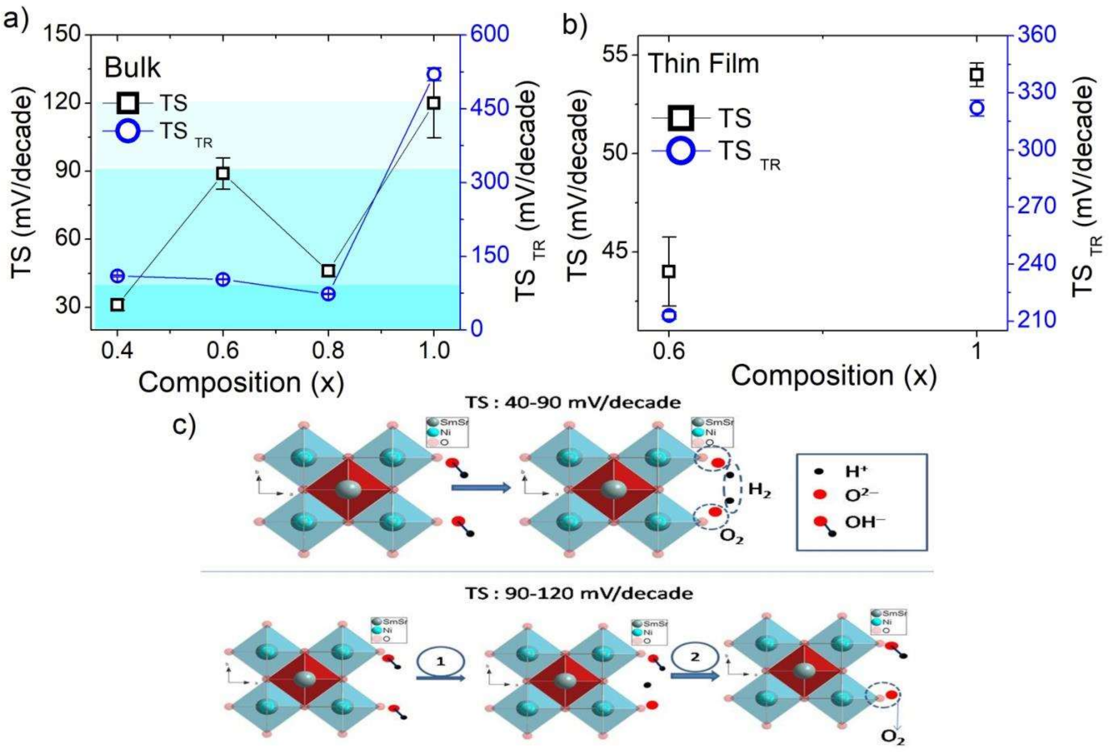

Figure 4.19: (a) Variation of Tafel slope (TS) at CR and transpassive region (TS_{TR}) with composition for bulk $Sm_{2-x}Sr_xNiO_{4-\delta}$ (b) Tafel slope at CR and transpassive region for $Sm_{2-x}Sr_xNiO_{4-\delta}$ (x = 0.6 and 1.0) thin films and (c) Mechanism for Oxygen evolution reaction with the variation in Tafel slope.

Fig. 4.19 (a) shows the variation of Tafel slope at CR and transpassive region with composition for bulk $Sm_{2-x}Sr_xNiO_{4-\delta}$ (b) Tafel slope at CR and transpassive region for $Sm_{2-x}Sr_xNiO_{4-\delta}$ (x = 0.6 and 1.0) thin films and (c) mechanism for oxygen evolution reaction will the variation in Tafel slope. It is observed that for bulk x = 0.6, Tafel slope is ~ 88 mV/decade (moderate electroactivity) and for bulk x = 1.0, Tafel slope is ~ 120 mV/decade (low electroactivity) while in case of thin films Tafel slope is 44 mV/decade and 54 mV/decade for x = 0.6 and 1.0, respectively i.e., lying between 40-90 mV/decade (moderate electroactivity). When the Tafel slope lies between 90-120 mV/decade, the electron transfer between the same active site is done step by step, in turn lowering the catalytic activity (Fig.4.19(c)). However, when the Tafel slope is 40-90 mV/decade, there is a scope of simultaneous four electron transfer in between active sites. This also suggests that x = 0.6 and 1.0 thin films along with bulk x = 0.6 have more active sites for the multiple electrons transfer instead of x = 1.0 bulk. Further, high Tafel slope for bulk x = 1.0 sample is approaching the highest Tafel slope of Pd nanosheets (585 mV/decade) [201] as illustrated in Table 4.4.

For bulk x = 1.0, higher Tafel slope is observed in comparison to other substituted samples. Various morphologies of Pd etc. are known to dissolute and form PtO, PdO on reaction with the H_2O and known to possess higher Tafel slope. Similarly, the $SmSrNiO_{4-\delta}$ electrodes are also shown to study the dissolution rate and NiO(OH) is formed in the present case. The illustration of the formation of NiO(OH) depends on x which changes the Ni in +3 state.

$$NiO + H_2O \rightarrow NiO(OH) + H^+ + e^- \qquad (4.3)$$

$$Ni_{Ni} + 2O \rightarrow V_{Ni}'' + 2V_O^{\bullet\bullet} + NiO_2 \qquad (4.4)$$

S. No	Sample	Electrolyte solution	Tafel Slopes	Ref.
1	Pd nanosheets	$0.5MH_2SO_4$+ 0.25M HCOOH	575mV/dec	[202]
2	Pd NPs -GO	$0.5MH_2SO_4$+ 0.25M HCOOH	405 mV/dec	[203]
3	Pd NP	$0.5MH_2SO_4$+ 0.25M HCOOH	585mV/dec	[204]
4	Concave nanocubes	$0.1MHClO_4$ +2M HCOOH	180 mV/dec	[205]
5	Pd/C synthesized at 393K	$0.5MH_2SO_4$+ 0.5M HCOOH	336mV/dec	[206]
6	Pd@Pt(100)	$0.1MHClO_4$ +50mM HCOOH	38/80 mV/dec at 0.15/0.18V	[207]
7	Pd nanocubes	$0.5MH_2SO_4$+ 0.5M HCOOH	133/205/286 mV/dec at 0.2/0.3/0.4V	[208]

8	Pd(111)/Pd(100)	0.1M$HClO_4$ +2M HCOOH	231mV/dec	[209]
9	Pd/RBPS/cubes/black	0.5M$HClO_4$ +0.5M HCOOH	188mV/dec	[210]
10	$Sm_{1.4}Sr_{0.6}NiO_{4-\delta}$	1 M Na_2SO_4	84mV/dec	in this work
11	$SmSrNiO_{4-\delta}$	1 M Na_2SO_4	120 mV/dec	in this work
12	$SmSrNiO_{4-\delta}$	1 M Na_2SO_4	520 mV/dec (transpassive region)	in this work
13	$Sm_{1.4}Sr_{0.6}NiO_{4-\delta}$ thin films	1 M Na_2SO_4	213 mV/dec (transpassive region)	in this work
14	$SmSrNiO_{4-\delta}$ thin films	1 M Na_2SO_4	322 mV/dec (transpassive region)	in this work

Table 4.4: A comparative of Tafel Slopes of commercial and well-known electrodes with the present work

Due to the change in oxidation state of Ni^{2+} to Ni^{3+} on air heating, its colour changes from light green of NiO to black colour of NiO(OH) (d-orbital tetrahedral complex). At x = 0.6, γ – NiO(OH) is observed while x = 1.0 is showing α-$Ni(OH)_2$ (Fig. 4.20). At x = 1.0, Ni-O signature in the fingerprint region ~500 cm^{-1} and hydroxyl groups above 2000 cm^{-1} are observed. Along with the different chemical environments, -OOH group is present at ~ 2000 – 2500 cm^{-1} [149] in x = 0.6 while -OH group at ~ 2900 cm^{-1} is present for x = 1.0. This supports our belief that the oxygen non-stoichiometry leads to structural change with different chemical environments. This is further confirmed through XPS measurements.

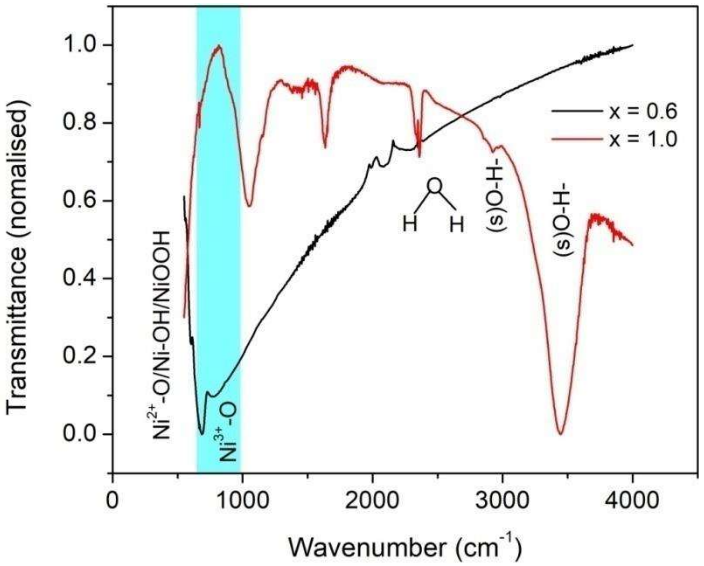

Figure 4.20: FTIR spectra of the samples $Sm_{2-x}Sr_xNiO_{4-\delta}$ at x = 0.6 and 1.0.

For the variable oxidation states of Ni and oxygen non-stoichiometry, XPS wide spectra and individual elemental spectra were calibrated with carbon correction appearing at 285 eV. Fig.4.21 represents the deconvoluted spectra using XPS peak 4.1 of Sm3d, Sr3d, Ni2p and O1s with Shirley background of the samples $Sm_{2-x}Sr_xNiO_{4-\delta}$ at x =0.6 and 1.0. In the wide spectrum , Ni and O auger peaks are observed along with the constituent elements as indexed according to the look up table (Fig.4.22). As observed, Sm 3d features are in accordance with the standard ones. Further, $Sr3p_{1/2}$ overlaps with C1s region in the wide spectrum and Sr 3d region has spin orbit coupling of 1.76 eV. However, in Sr multiple chemical states are present with the formation of oxides and carbonates as Sr readily reacts with O_2 and CO_2 present in atmosphere. In the present case too, oxide and carbonate spin – orbit coupling is observed. In the Ni component, Ni2p has split spin –orbit component at ~17.3 eV with complex shape as mixture of metal, oxide, hydroxide and satellite features. In the present case, multiplet splitting of Ni(metallic), NiO and $Ni(OH)_2$ or Ni(OOH) are observed for both the samples suggesting the different Ni states. In x = 0.6, the intensity of Ni (metal) and $Ni(OH)_2$ are higher in comparison to x = 1.0 sample. The deconvoluted XPS spectra for O1s indicates metal-O, metal hydroxide peaks ad auger peaks. For x = 0.6, metal –O peak has higher intensity in comparison to x = 1.0 while metal –hydroxide peak has higher intensity for x = 1.0. Further auger peak of O in x = 1.0 has lower intensity than that of x = 0.6. This is suggesting that vacancy formation is more in x = 0.6 rather than vacancy adsorbed in x = 1.0. This is in accordance with the δ calculation from TGA measurements. However, there is no shifting in Sm3d and Sr3d peaks while, Ni-O and metal-hydroxide peaks are observed to shift suggesting the change in oxidation states of Ni^{2+} to $Ni^{2+\delta}$ and O^{-2} to $O^{-2-\delta}$ [211]–[214]. Further, the satellite peak of Ni is interacting with the auger peak of O leading to the reduction in oxygen vacancy (through electron consumption visible in reduced intensity of Auger) in x = 1.0 sample. Thus, Ni-O (p-d interaction) bond is playing critical role in the electrohemical reversibility. The conversion of Ni^{3+} to Ni^{2+} with the addition of electron in e_g set of orbitals in octahederal splitting leads to electron intercalation with the change in x. This electron intercalation and oxygen addition via interstitial sites indicates different mechanisms of electrocatalysis with x as chemical environment changes. Thus, higher oxygen adsorption in x = 1.0 as compared to x = 0.6 leads to more number of electron transfer in electrocatalysis.

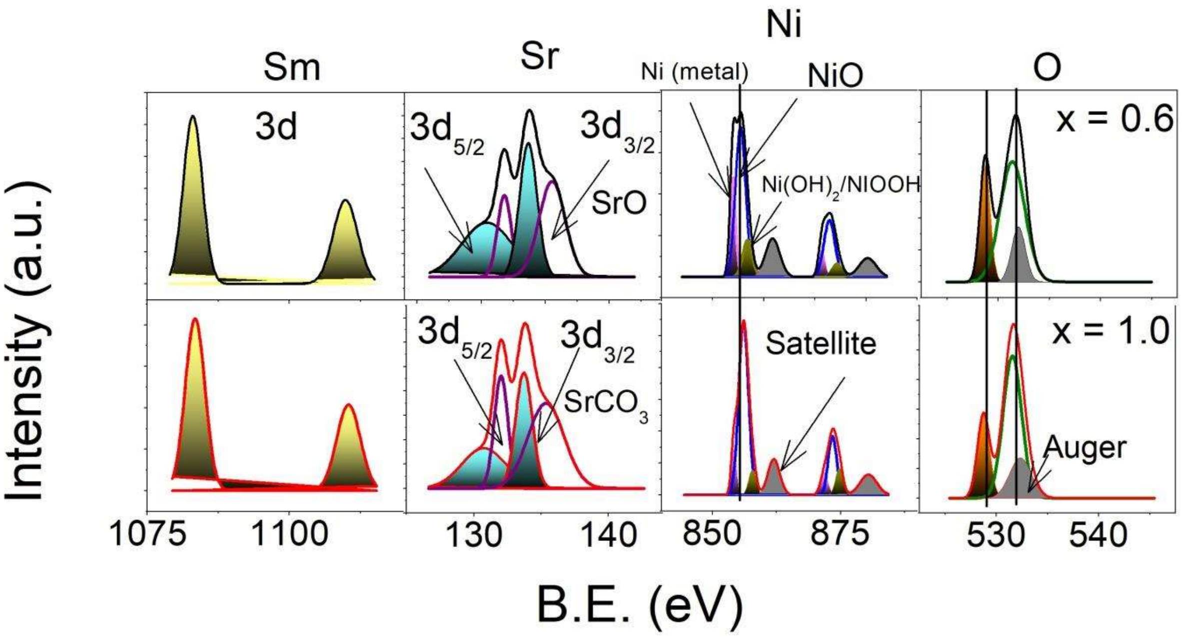

Figure 4.21: Deconvoluted XPS spectra using XPS peak 4.1 of Sm3d, Sr 3d, Ni2p and O1s with Shirley background of the samples $Sm_{2-x}Sr_xNiO_{4-\delta}$ at x = 0.6 and 1.0

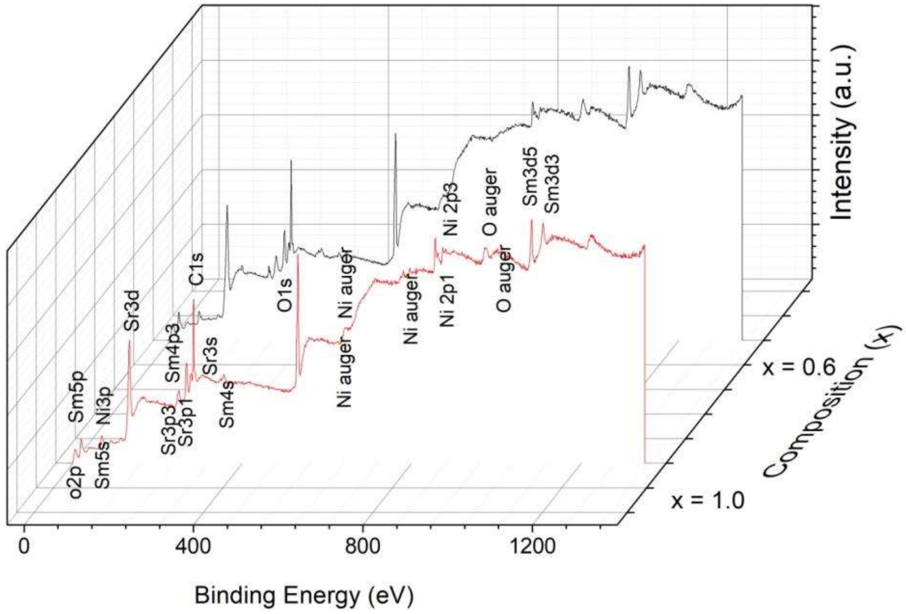

Figure 4.22: Wide XPS spectra of the $Sm_{2-x}Sr_xNiO_{4-\delta}$ (x = 0.6 and 1.0)

Further, the orthorhombic and tetragonal structure of $SmSrNiO_{4-\delta}$ has different magnetic and charge ordering depending on the modulation wave number, ε [151]. The modulation wave number depends upon doping index and Sr doping and hence influencing the charge ordering[151]. This charge ordering difference in the two structures (orthorhombic for x = 0.6 and tetragonal for x = 1.0) leads to the change in rate constant of the voltammograms (different redox species). Thus, different number of electron transfer mechanisms is observed with the structure due to the different charge ordering in charge transfer processes.

The chronoamperometric response is studied for x = 0.6 and 1.0 sample and thin films (Fig. 4.23). The transient current decay time estimated using exponential decay fitting of the current vs time graph is τ = 1505 sec for x = 0.6 sample and τ = 0.328 sec for x = 0.6 thin film. Further, for x = 1.0, the value of τ is 0.223 sec. Thus, x = 1.0 thin film is more suitable as nanoelectrode owing to its low transient time and electrochemical reversibility.

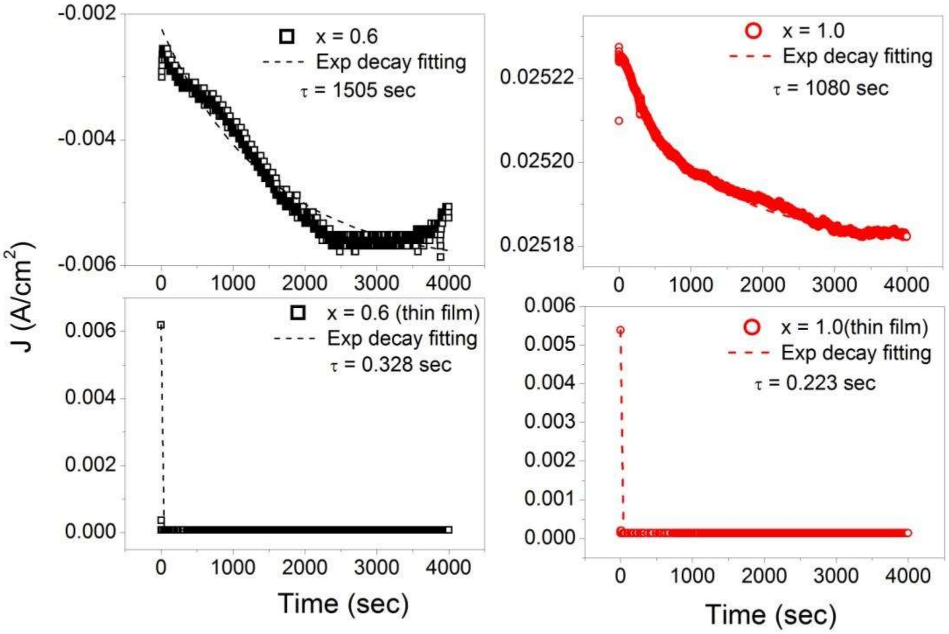

Figure 4.23: Chronoamperometric response showing transient decay tie for the x =0.6 and 1.0 thin films.

On a comparative note, we have studied the reversibility mechanisms of x = 0.6 and 1.0 sample and thin films and found that the reversibility mechanism is due to diffusion in case of sample while in thin films it is governed by adsorption. Further, CR has increased in x = 1.0

thin film with the reduction in transient response proving its suitability as nanoelectrode. This can be further attributed to the increase in lattice mismatch with the phase change.

4.4 Conclusion

A series of $Sm_{2-X}Sr_XNiO_{4-\delta}$ (x = 0.0 to 1.0) was successfully prepared using conventional solid-state route method with the change in structure at ~ x = 0.8. The minimum oxygen non-stoichiometry for x = 0.6, while composition with x = 0.8 is maximum oxygen deficient. The conversion from $4e^-$ (for x = 1.0) to $2e^-$ (for x = 0.6) transfer mechanism is observed with the different irreversibility index for the bulk sample. It is observed that for bulk x = 0.6, Tafel slope is ~ 88 mV/decade (moderate electroactivity) and for bulk x = 1.0, Tafel slope is ~ 120 mV/decade (low electroactivity) while in case of thin films Tafel slope is 44 mV/decade and 54 mV/decade for x = 0.6 and 1.0, respectively i.e., lying between 40-90 mV/decade (moderate electroactivity). Further, the lattice mismatch increase with phase change consequently enhances the number of active sites proving the suitability of x = 1.0 (i.e., $SmSrNiO_{4-\delta}$) thin film as Nanoelectrocatalyst in neutral medium.